Article

Structure

Cryo-Electron Microscopy Structure of Human Peroxiredoxin-3 Filament Reveals the Assembly of a Putative Chaperone

Graphical Abstract

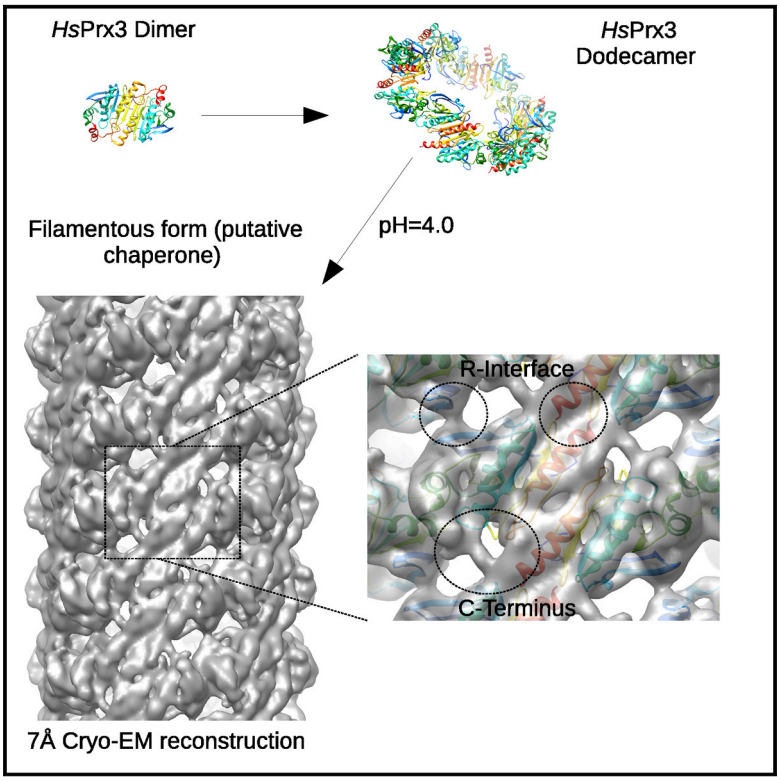

Highlights

- We report a ~7-Å resolution cryo-EM 3D reconstruction of helical *Hs*Prx3 filaments
- First structure of the long high-molecular-weight (HMW) form of 2-Cys Prx
- In contrast to previous studies, the HMW form houses a partially folded C terminus
- Hydrophobic patches in the lumen of HMW *Hs*Prx3 may bestow holdase activity

Authors

Mazdak Radjainia, Hariprasad Venugopal, ..., Juliet A. Gerrard, Alok K. Mitra

Correspondence

a.mitra@auckland.ac.nz

In Brief

Radjainia et al. describe an approximately 7-Å structure of the human peroxiredoxin3 (*Hs*Prx3) filament. Dodecameric toroids of *Hs*Prx3 self-associate to form filaments that have putative chaperone activity. A pseudo-atomic model derived from the cryo-EM map provides insight into toroid stacking and clues to the chaperone activity.

Radjainia et al., 2015, Structure *23*, 912–920
May 5, 2015 ©2015 Elsevier Ltd All rights reserved
http://dx.doi.org/10.1016/j.str.2015.03.019

CellPress

Structure
Article

Cryo-Electron Microscopy Structure of Human Peroxiredoxin-3 Filament Reveals the Assembly of a Putative Chaperone

Mazdak Radjainia,[1,8] Hariprasad Venugopal,[1,8] Ambroise Desfosses,[1] Amy J. Phillips,[2,3,4] N. Amy Yewdall,[3,4] Mark B. Hampton,[5] Juliet A. Gerrard,[1,3,4,6,7] and Alok K. Mitra[1,*]

[1]School of Biological Sciences, University of Auckland, Private Bag 92019, Auckland 1010, New Zealand
[2]Izon Science Limited, 8c Homersham Place, Burnside, Christchurch 8053, New Zealand
[3]Biomolecular Interaction Centre and School of Biological Sciences, University of Canterbury, Private Bag 4800, Christchurch 8140, New Zealand
[4]MacDiarmid Institute for Advanced Materials and Nanotechnology, Victoria University, Wellington 6140, New Zealand
[5]Centre for Free Radical Research, Department of Pathology, University of Otago Christchurch, Christchurch 8011, New Zealand
[6]School of Chemical Sciences, University of Auckland, 23 Symonds Street, Auckland 1010, New Zealand
[7]Callaghan Innovation Research Limited, Lower Hutt 5040, New Zealand
[8]Co-first author
*Correspondence: a.mitra@auckland.ac.nz
http://dx.doi.org/10.1016/j.str.2015.03.019

SUMMARY

Peroxiredoxins (Prxs) are a ubiquitous class of thiol-dependent peroxidases that play an important role in the protection and response of cells to oxidative stress. The catalytic unit of typical 2-Cys Prxs are homodimers, which can self-associate to form complex assemblies that are hypothesized to have signaling and chaperone activity. Mitochondrial Prx3 forms dodecameric toroids, which can further stack to form filaments, the so-called high-molecular-weight (HMW) form that has putative holdase activity. We used single-particle analysis and helical processing of electron cryomicroscopy images of human Prx3 filaments induced by low pH to generate a ~7-Å resolution 3D structure of the HMW form, the first such structure for a 2-Cys Prx. The pseudo-atomic model reveals interactions that promote the stacking of the toroids and shows that unlike previously reported data, the structure can accommodate a partially folded C terminus. The HMW filament lumen displays hydrophobic patches, which we hypothesize bestow holdase activity.

INTRODUCTION

Prxs are a ubiquitous class of thiol-dependent peroxidases found in all biological kingdoms. Prxs play an important role in protecting cells from oxidative stress and their catalytic mechanism has been well characterized. Prxs catalyze the detoxification of hydroperoxides including hydrogen peroxide and peroxynitrite and are an essential component of the antioxidant defense system. Loss of Prx function has been suggested in many diseases including Alzheimer's, Parkinson's, various cancers and age related disease, wherein oxidative stresses are evident (Hofmann et al., 2002). Prxs also can assume complex oligomeric structures that bestow the potential for these proteins to play a role in cell signaling and act as chaperones (Winterbourn and Hampton, 2008; Wood et al., 2002).

A number of crystal structures of Prxs have been reported (Hall et al., 2009). In the case of the so-called typical 2-Cys Prxs, the protein is arranged as an antiparallel homodimer. A hydroperoxide first oxidizes the peroxidatic cysteine (Cys_p) in one monomer, which then engages the resolving cysteine (Cys_r) in the partner monomer to form an intermolecular disulfide bond. The conversion of the disulfide-bonded dimers back to the reduced state is carried out by thioredoxin. Humans express six Prx isoforms: *Hs*Prx1–4 are typical 2-Cys Prxs, with Prx3 specifically located in the mitochondrial matrix; *Hs*Prx5 is an atypical 2-Cys Prx and *Hs*Prx6 is a 1-Cys Prx. Prxs associate into ring-like (toroidal) assemblies comprising either five or six Prx homodimers. These decameric or dodecameric toroids are referred to as the low-molecular-weight (LMW) species. LMW Prxs can self-assemble to high-molecular-weight (HMW) species (Wood et al., 2003; Harris, 1968) including stacks of varying numbers of Prx toroids, which have been visualized by X-ray crystallography and electron microscopy (Gourlay et al., 2003; Saccoccia et al., 2012; Phillips et al., 2014). These HMW forms are of great interest because they are considered to possess holdase activity, i.e. act as chaperones that counteract protein aggregation by binding unfolded proteins (Kumsta and Jakob, 2009). A recent study by Teixeira et al. (2015) suggests that an LMW species in the parasite *Leishmania infantum* can also protect against heat-stress-mediated protein unfolding.

Formation of the HMW form is promoted by the hyperoxidation of Cys_p to the sulfinic and sulfonic forms by H_2O_2. This results in the loss of peroxidase function. Saccoccia et al. (2012) showed that an acidic environment also causes this HMW formation. In addition to a putative biomedical relevance, the ability of Prxs to form such organized supramolecular HMW assemblies in a switch-like fashion makes them an attractive candidate for application in protein nanotechnology (Phillips et al., 2014). For instance, Ardini et al. (2014) demonstrated the use of Prx tubes

 ©2015 Elsevier Ltd All rights reserved

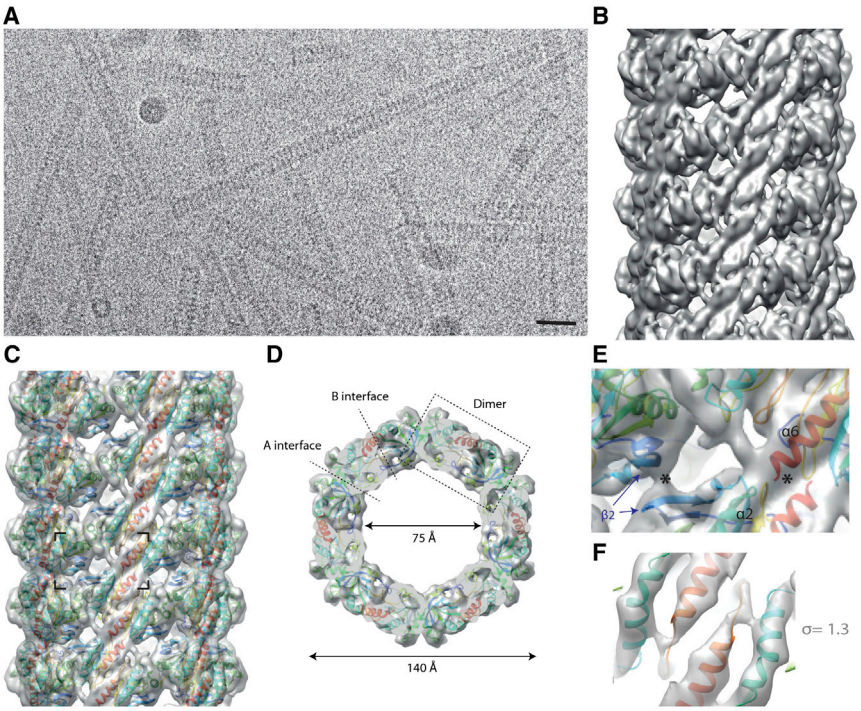

Figure 1. Cryo-EM Reconstruction of *Hs*Prx3 Filaments

(A) Cryo-EM micrograph shows a collection of *Hs*Prx3 nanotubes formed by acidification of a purified protein sample.

(B) 3D reconstruction of the helical nanotubes comprised of helically arranged toroidal dodecamers with helix parameters of 42.82 Å for the axial and azimuthal rotational angle of 8.06°. The map has an estimated resolution of 7.4 Å and is rendered at 1σ of the map density using UCSF Chimera (Pettersen et al., 2004).

(C) The cryo-EM reconstruction of *Hs*Prx3 filament docked with a homology model for *Hs*Prx3 derived using the X-ray crystal structure of *Bt*Prx3 (PDB: 1ZYE).

(D) An edge-on view for an excised toroid of the helix showing the A and B interfaces and the dimer repeat.

(E) The adjacent toroids are associated via the R interface (*). The density volumes harboring the α2, α6, and β2 strand are indicated showing good agreement of the BtPrx3 crystal structure-derived *Hs*Prx3 pseudo-atomic model.

(F) Volume rendered at 1.3σ of the map density to highlight the strongest density in the map, to show how α helices are resolved.

as nano-peapods for ultra-small gold particles, which could be useful as nanowires.

Currently, the only detailed structural information for the HMW form is provided by a recently reported crystal structure of the so-called chaperone species of *Schistosoma mansoni* Prx1 (*Sm*Prx1; Saccoccia et al., 2012 [PDB: 3ZVJ]), which is composed of a stack of two decameric rings (i.e. five Prx dimers) formed at an acidic pH (pH 4.2). These authors deduce conformational changes in Prx involving most notably the presumed unfolding of the C terminus at the catalytic site where Cys_p and Cys_r reside. It was postulated that as a result of this unfolding, a hydrophobic surface of Prx is exposed, which facilitates binding of unfolded substrates. More specifically, it was suggested that unfolded substrates bind primarily to the hydrophobic pocket at the unfolded catalytic site and to a lesser extent to the unfolded C terminus. Chaperone activity assays showed decreasing holdase activity with increasing length of stacks (Angelucci et al., 2013) suggesting that substrate binding might only occur at the rims of stacks in a GroEL-like fashion. Unfolding of the C terminus was suggested to be a steric requirement for stacking, which otherwise would destabilize the R interface formed by the α2 and α6 helices of the next toroid, which stabilizes the toroid stack (Saccoccia et al., 2012). However, it is not clear why chaperone function, presumably mediated by such hydrophobic patches at the catalytic sites, would be restricted only to Prx stacks, since unfolding of the catalytic site can also occur in LMW species or even in Prx dimers. It was hypothesized that holdase activity and stacking work cooperatively since the stacked state requires unfolding.

This leads to the question as to why the toroids associate into long nanotubes. Although the crystal structure of *Hs*Prx3 toroid has not yet been solved, the available structure of the bovine homolog (*Bt*Prx3), which shares 93% sequence identity with *Hs*Prx3, is considered to be representative of the structure of *Hs*Prx3. *Bt*Prx3 shows some unusual structural features in that, whereas most of the other 2-Cys Prxs display decameric oligomers composed of five dimers, *Bt*Prx3 forms a dodecamer. We have shown that, likewise, *Hs*Prx3 also forms dodecamers as well as double stacks of dodecamers analogous to *Sm*Prx1 chaperone species, both of which display D6 symmetry. The seemingly facile assembly of the *Hs*Prx3 nanotube raises the possibility of an as yet unknown additional biological function for such long filaments, which could be distinct from the function of *Sm*Prx1 double stacks. These large assemblies with varying lengths are refractory to analysis by X-ray crystallography but are particularly well suited for single-particle cryo-electron microscopy (cryo-EM) analysis. We asked if these filaments are conformationally distinguished from the reported double-stack structure. For this purpose, and in order to better understand the molecular interactions that promote assembly, we describe here for the first time, high-resolution 3D reconstruction at ~7 Å obtained by cryo-EM of long ordered HMW *Hs*Prx3. We compare the cryo-EM derived structure with the crystal structure of *Sm*Prx1 double stacks, called DS hereafter to differentiate between the long HMW nanotube of *Hs*Prx3 reported here. We describe and discuss conformational alterations in the Prx toroid that facilitate and stabilize the filamentous architecture and show that the *Hs*Prx3 filament displaying distinctive conformational features is more representative of the chaperone species of the 2Cys prx family than the DS of *Sm*Prx1.

RESULTS

We focused on the recently described long filaments of *Hs*Prx3 (Phillips et al., 2014), which form at pH4, in order to gain structural insights into the longest yet observed HMW assembly of Prxs. A typical field of *Hs*Prx3 nanotubes suspended in vitrified buffer is shown in a cryo-EM micrograph (Figure 1A). The power

Table 1. Image Processing Statistics	
Pixel size on the specimen, Å	1.26
Number of filaments selected	8,656
Number of segments included	7,772
Segment size, Å	431
Segment step size, Å	214
Number of asymmetric units included in final reconstruction	466,320
Resolution in Å at FSC = 0.143	7.4
Helical rise, Å	42.82
Helical rotation, °	8.06

spectrum of class averages of cryo-EM images suggested that the *Hs*Prx3 filaments are helical in nature. In order to fully characterize the helical assembly, we first carried out projection-matching-based single-particle reconstruction using a solid cylinder as the initial model. The 6-fold symmetry, as evident in the end-on views of toroids (the building block of the tubes) was imposed throughout this refinement. This process resulted in an intermediate ~10-Å resolution reconstruction (Figure S1A) that displayed clearly the helical nature of the 3D structure. We used this reconstruction to determine the helical symmetry using a real-space autocorrelation method (Heymann et al., 2013), which yielded an initial estimate for the axial rise of 42.7 Å and azimuthal rotation angle of 7.9° (Figure S1B). The helical parameters were then refined using the iterative helical real-space reconstruction (IHRSR) approach (Egelman, 2000), which applies search and enforcement of helical symmetry, varying the values for axial rise and azimuthal rotation around the initial estimates. The helical parameters converged to a stable solution at 42.8 Å for the axial rise and 8.1° for the azimuthal rotation angle irrespective of the choice of initial pair (Figures S1C and S1D). The resultant reconstruction with these refined helix parameters clearly showed the presence of the additional 2-fold symmetry axis perpendicular to the helix axis (D6 symmetry), as present in the *Bt*Prx3 crystal structure (PDB: 1ZYE), and therefore this symmetry was imposed in further steps of the refinement. To obtain the final high-resolution reconstruction, we used the software SPRING (Desfosses et al., 2014), which exploits alignment restraints adapted to helical geometry and an improved symmetrization procedure (Desfosses et al., 2014). Again, starting with a featureless cylinder as the initial model, we obtained the final 3D reconstruction (Figure 1B); the projection-derived power spectrum agreed well with the cumulative power spectrum of the aligned images (Figure S2A). This reconstruction had an estimated resolution of 7.4 Å, using the Fourier shell correlation (FSC) = 0.143 criteria between two independently refined reconstructions from half dataset (gold standard FSC) (Figure S2B). The resolution estimated using SPRING (Desfosses et al., 2014) for the full dataset was 6.7 Å. Table 1 provides details of statistics for the image processing exercise.

The ~7-Å resolution cryo-EM density map of a human Prx3 filament produced by low pH treatment is shown in Figure 1B. We applied rigid-body docking of monomers from the available Prx crystal structures to generate a set of pseudo-atomic models for the helical assembly of *Hs*Prx3. These homologous, pseudo-atomic models were utilized as a framework for revealing pertinent features of the 3D structure. In each case of the docking exercise, a Prx monomer extracted from a given crystal structure was fitted into a toroid using the symmetry fit module in UCSF Chimera (Pettersen et al., 2004) at a resolution cutoff of 7 Å using the D6 and the helical symmetry to populate the map with symmetry-fitted copies. Initial rigid-body docking analysis used a homology modeled monomer of *Hs*Prx3 using the *Bt*Prx3 crystal structure as the template in ITASSER (Zhang, 2008). Figure 1C shows the cryo-EM reconstruction fitted with the symmetric copies of the various homologous monomer models. To see the fit in detail, we excised an individual toroid from the filament reconstruction. In its end-on view, each individual toroid is composed of six dimers (Figure 1D) showing that the filament has an inner diameter of 75 Å and an outer diameter of 140 Å. The interdimer A interface and the intermonomer B interface are clearly visible (Figure 1D) and, importantly, the inter-toroid R interface, which is thought to drive the stacking, as reported by Saccoccia et al. (2012). Even with a threshold to highlight only the high-density regions, the quality of the map is sufficient to identify individual α-helices and the tertiary fold is clearly discernible (Figure 1E). This allowed for detailed comparison and elaboration of conformational rearrangement with respect to the known X-ray crystal structures.

We compared our reconstruction to the known crystal structure of *Bt*Prx3 (PDB: 1ZYE). At the global level, we first examined and compared the inner diameter of the fitted toroid generated by symmetric fitting of monomers of *Bt*Prx3 to that for the crystal structure of *Bt*Prx3 (Figure 2A). We note that the *Bt*Prx3 toroid is not uniform in diameter. The inner diameter in the crystal structure, when measured as the distance between C^{α} of opposing pairs of residues, Gly117 in chain A and chain D is 80.6 Å in one direction and that between Pro2 in chain J and chain F is 75.6 Å in the second direction (Figure 2A). The inner diameter for the pseudo-atomic model for the 3D reconstruction, generated using *Bt*Prx3 monomer (chain H) and measured using the same atom pairs, was 83.2 and 83.5 Å in the analogous directions. This presents a systematic difference between the cryo-EM map and the crystal structure, for which noncrystallographic symmetry was not imposed. Even if a crystallization artifact accounts for the difference, it still shows that the configuration of the toroid can vary. In fact, our observation that *Hs*Prx3 can access a toroidal configuration with a wider conformation is noteworthy in view of the postulation of a smaller tight and a wider loose conformation (Hall et al., 2011).

Next we asked whether the change in diameter is accompanied by conformational changes at the various Prx interfaces (Figure 2B). For this purpose, we extracted triplets of adjacent chains encompassing the A and B interface from the *Bt*Prx3 crystal structure and compared these with those extracted from the aforementioned pseudo-atomic model of the toroid in the cryo-EM map. The cross-superimposition of the two sets of monomer triplets indicated only subtle differences at the B interface (root-mean-square deviation [rmsd] 1.3 Å) but significantly larger changes (rmsd 2.1 Å) at the A interface, which thus appear to control the curvature of the toroid. On the other hand, when the corresponding section extracted from the cryo-EM map is compared with that in the crystal structure of the *Sm*Prx1 chaperone species, our reconstruction shows strong similarities at the A and R interfaces (Figure 2). When

 ©2015 Elsevier Ltd All rights reserved

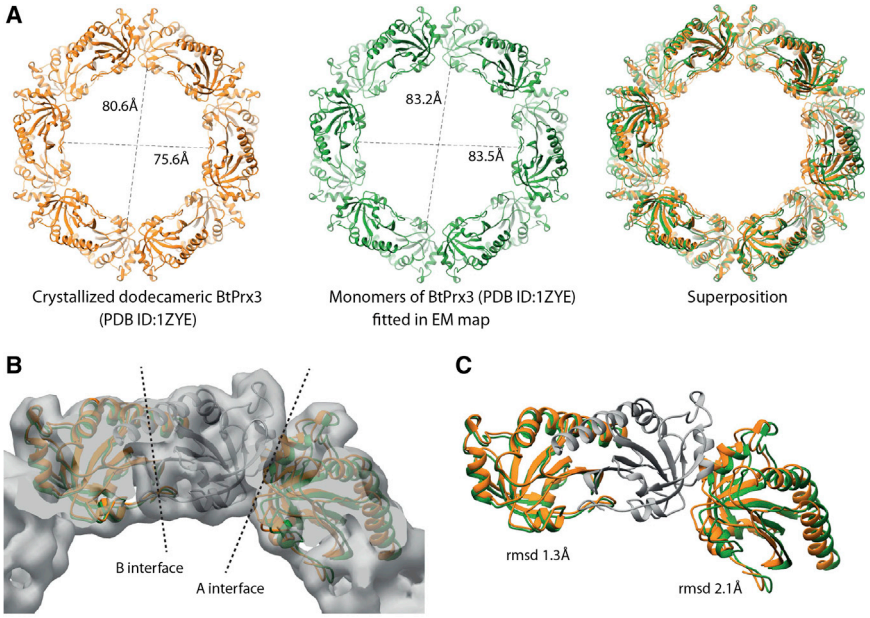

Figure 2. Comparison of the Crystal Structure of *Bt*Prx3 with the Pseudo-atomic Model Derived from the Cryo-EM Reconstruction of *Hs*Prx3 Filament

(A) Inner diameter of the *Bt*Prx3 toroid in the crystal structure was measured as the distance between Cα of opposing pairs of residue Gly117 in chain A and chain D (80.6 Å) and that between Pro2 in chain J and chain F (75.6 Å). In the pseudo-atomic model of *Hs*Prx3, the corresponding diameters are 83.2 and 83.5 Å, respectively, for the same atom pairs. Thus, the asymmetric dodecameric *Bt*Prx3 toroid in the crystal structure has one of the calculated diameters significantly shorter than that in the *Hs*Prx3 toroid (75.6 Å compared with 83.5 Å). The right-most panel shows the superposition of the *Bt*Prx3 (orange) and *Hs*Prx3 (green) toroids.

(B and C) The changes in the toroid assembly is due to somewhat larger rearrangement at the interdimer A interface compared with the B interface (rmsd of 2.1 and 1.3 Å, respectively) when triplets of monomers for the crystal structure of *Bt*Prx3 and that for the corresponding *Hs*Prx3 pseudo-atomic model are superimposed for comparison.

compared with the DS structure, the pseudo-atomic model derived from the 3D reconstructed density map of HMW showed interesting similarities at the R interface but significant differences at the B interface, which includes the C terminus. We discuss below further pertinent structural features gleaned from the analysis of the 3D reconstructed density map guided by the pseudo-atomic model.

Conformational Features at the R Interface

At the R interface, adjacent toroids in the *Hs*Prx3 filament and described by the aforementioned pseudo-atomic model display interactions between opposing α2 and α6 helices and β2 strands, indicating similar molecular interactions as seen for the *Sm*Prx1 chaperone species. This mode of interaction shared by DS and HMW suggests that stacking is driven primarily by the R interface. The conservation of several key residues that constitute the R interface across species is in line with the HMW structure being biologically relevant. Considering the DS as a fragment of a helical filament, evaluation of the helix parameters of the DS species showed that the values for the axial rise of 40 Å and azimuthal rotation angle of 10° are comparable with those for the *Hs*Prx3 filament (42.8 Å and 8.1°). The difference might be attributed to the 5-fold symmetry rather than the 6-fold symmetry seen in the HMW form. The consequence of this alteration on the precise interactions that happen in the R interface needs to be ascertained by higher-resolution data.

Conformational Features at the B Interface

The intra-dimer interface is designated as the B interface describing the intermonomer interactions at the luminal and external faces of the toroid and those at the middle of the dimer. Analogous to the *Bt*Prx3 structure, many of the features of the B interface are conserved in the pseudo-atomic model for the cryo-EM map. At the luminal face, the observed density shows the short β-hairpin as well as the α5 helix. At the middle of the interacting dimer face, a continuous β-sheet is formed by antiparallel β7 and β7′ strands. On the external face, however, significant changes are observed at the C terminus compared with that in the DS species of *Sm*Prx1 reported by Saccoccia et al. (2012). These authors report that the stacking of the toroids is concomitant with disordering of the C-terminal region based on their observation that there is no corresponding density in the crystal structure. In our map we see density to the left of the α6 helix (Figure 3) that links α6 to the α2 and α3/α4 helix in the partner monomer. This clear volume of density is attributable to a considerable portion of the C terminus, which is not present in the *Bt*Prx3-derived homology model (Figure 3A). Upon comparing the DS crystal structure and the *Hs*Prx2 crystal structure with our map (Figures 3B and 3C), we see that the C-terminal helix analogous to that seen in *Hs*Prx2 could be well accommodated in our map, with some rearrangement. Rigid-body docking of monomers extracted from the crystal structure of *Hs*Prx2 (PDB: 1QMV), shows that the loop region of the C terminus that interacts with α6, where the conserved W233 resides (Figure 3C), is well within the aforementioned volume of density in our cryo-EM reconstruction but the rest of the C-terminal loop is not fully resolved in our reconstruction, hinting that this section of the C terminus loop may be flexible or adopting different conformations. Based on our reconstruction, the C terminus appears to be interacting with helix α2′ and the α3′/α4′ region. Although the ~7-Å resolution achieved does not clarify the atomic details of this interaction, it is of note that a similar interaction was previously reported in the structure of *Hs*Prx4 (PDB: 3TJB) as one example where the C-terminal region ends in an α helix. This helix is a major feature of the eukaryotic 2-Cys Prxs and is characterized by the conserved YF motif in their C terminus. At the C terminus, the amino acid sequence of *Sm*Prx1 is distinct from *Hs*Prx1, *Hs*Prx2, *Bt*Prx3, *Hs*Prx4, and *Hs*Prx3 (Figure 3D). Sequence alignment shows that *Sm*Prx1, while being very similar overall to the rest of the polypeptide chain such as

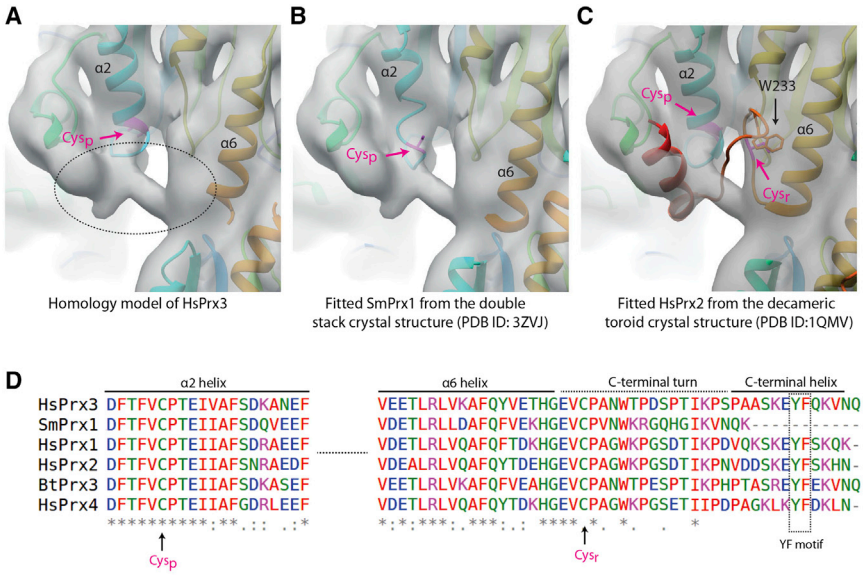

Figure 3. Close-up of the Cryo-EM Map of *Hs*Prx3 Filament Elaborates Density for a Part of the C Terminus

(A–C) The region of the 3D map around the density attributed to the C terminus (dashed ellipse). The docked homology model (A), the SmPrX1 (DS) X-ray crystal structure model (PDB: 3ZVJ) (B), and the decameric *Hs*Prx2 X-ray crystal structure (PDB: 1QMV) model (C) docked in the 3D map of the *Hs*Prx3 filament. Based on the comparison of (A) and (C), the terminal α helix can be accommodated in (A). As indicated in (C), a part of the density attributable to the C-terminal loop indicated by the location of W233 can be identified.

(D) Comparison of the amino acid sequences for SmPrx1 and 2-Cys peroxiredoxins at the C terminus shows the absence of the YF motif-containing terminal α helix.

the sequence composition of the α2 and α6 helices, which are part of the R interface, lacks the 10–11 amino acids including the conserved YF motif at the C-terminal end. Therefore, the DS-derived hypothesis that the unfolded C terminus is a requirement to facilitate the R interface mediated HMW formation may not apply due to systematic departure at the amino acid sequence level.

Role of the C Terminus in the Assembly of the HMW Form

The importance of the C terminus in oligomerization is suggested by the fact that C-terminal deletion mutants fail to form the HMW species under oxidative stress (Jang et al., 2004; Moon et al., 2005). Mutation of Cys_r has been shown to increase the susceptibility of 2-Cys Prxs to hyperoxidation and these molecules also readily form HMW oligomers, as is the case with yeast Prx1 for Cys_r to serine mutation (Jang et al., 2004).

In light of the importance of the C terminus in HMW formation, we investigated in detail the density volume attributed to this region in our map. The 3D map was analyzed using UCSF Chimera to examine the volume density gradient, which can be related to local resolution and therefore can be informative of conformational heterogeneity and/or disorder (Figure 4B). This exercise showed that the densities corresponding to helices α6 and α2 are clearly resolved and hence are indicative of ordered segments. The α helix at the C-terminal extremity and the loop region of the C terminus, potentially interacting with α6, were relatively less resolved as was the bridging density between α6 and α2, which could be occupied by the remaining part of the C terminus. These could be representative of disorder in this region of the polypeptide chain. This lack of clarity in the definition of some regions of the C-terminal loop is potentially interesting especially in the light of the recent finding by Wang et al. (2012) for *Hs*Prx4 (PDB: 3TKS). These authors observe that upon oxidation of Cys_p, the C terminus and the α2 helix become progressively rigid as indicated by the crystallographic B factor. This observation assumes significance vis-à-vis our observations for the C-terminal region of *Hs*Prx3 because the only reducing environment that the protein experienced was during the cleavage of the His-tag and subsequently the protein sample was maintained under a nonreducing condition. This makes the assessment of the exact oxidative state of each monomer in the filament difficult, hence opening up the possibility that the C-terminal region may be conformationally heterogeneous dependent on the oxidative state of Cys_p leading to the lack of definition in some part of the C-terminal loop. In light of the study by Wang et al. (2012), we also looked at the possible influence of the C-terminal conformational heterogeneity at the R interface formed by α6 and α2 of apposed toroids (Figure 4A). As reflected in the B factors, the conformational rigidity in the α2 and C-terminal helix in the oxidized form of *Hs*Prx4 also translates to more order in the C-terminal end of α6. It is therefore possible that the process of hyperoxidation that promotes the observed rigidity in the active site translates to a reduced flexibility, extending to the whole of the R interface. Such a scenario could also be in play in the low pH-induced oxidized state in *Hs*Prx3 that facilitates the formation of long, highly ordered nanotubes.

DISCUSSION

Prxs are clearly very significant proteins in biology, as demonstrated by their abundance in most living cells. Despite a large body of research, many details of Prx structure and function remain unclear, especially the structure-function relationship of the HMW form. Oxidative stress is reported to be the major trigger for the formation of these HMW forms. The only structural data available for a DS HMW form is that for the *Sm*Prx1 DS (Saccoccia et al., 2012), in which it is proposed that lowering the pH to below the pK_a of Cys_p (~5) results in destabilization of the ionic interaction of Arg124 with Cys_p, which in turn allows the Cys_p to assume a conformation that is similar to that when it is hyperoxidized. For *Sm*Prx1, the stacking of the decamers in DS is stabilized by polar contacts between helices α2, α6 and the β2 strands in the monomers belonging to the two apposing toroidal rings. Comparison of this DS structure with the corresponding Prx1 LMW form of *S. mansoni* revealed that the elaboration of these new contacts is concomitant with

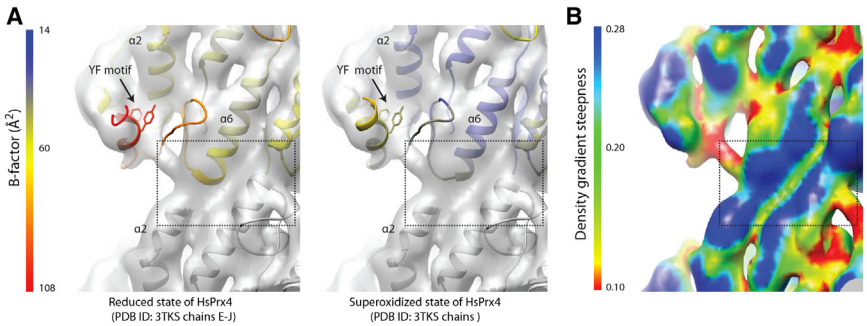

Figure 4. Role of the C-Terminal Helix in Stabilizing the R Interface

(A) *Hs*Prx4 X-ray structures (PDB: 3KTS) in the reduced and hyperoxidized state (Wang et al., 2012) docked in the 3D cryo-EM map with the C^{α} trace color coded to reflect the crystallographic B factor (left and middle panel). The terminal α helix and the YF motif are shown. The B factor distribution suggests that stabilization of the C-terminal helix in the oxidized form, mimicked by the low pH, can improve the stability of the R interface contributing to the stacking of the *Hs*Prx3 toroids. (B) The right-most panel displays the 3D map color coded according to density gradient and indicates good resolution for the R interface (indicated by the rectangle). The existence of a C-terminal helix in our structure may explain why *Hs*Prx3 can form much longer filaments than what was observed for *Sm*Prx1, which does not have a YF motif (Figures 3A and 3D).

conformational changes at three sites: (1) local unfolding (LU) in the C terminus within the first turn of α2 at the catalytic site, similar to structural changes that accompany oxidation of Cys_P; (2) a rotation in the orientation of dimers within the toroid that bring apposing α2/α6 helices together; and (3) a perturbation of the intra-dimer interaction at the B interface. The authors suggested that these conformational changes are required for favorable steric interactions to enable the formation of the DS species. Furthermore, elucidation of the conformational changes at the R interface led to a possible explanation for the holdase activity of Prx HMW forms. Thus, it was proposed that the unfolded regions in a toroid stack could provide such a hydrophobic patch (Saccoccia et al., 2012). Chaperone activity assays showing reduced holdase efficiency with increased length of stacks suggested that only the extremities of HMW have holdase function (Angelucci et al., 2013).

Although difficult to hyperoxidize (Cox et al., 2009; Haynes et al., 2013), *Hs*Prx3 is a target for sulfiredoxin, which scavenges the hyperoxidized Cys_p, and has been implicated in adrenal steroidogenesis (Kil et al., 2012) under oxidative stress. In the present study, we mimicked the hyperoxidized state by subjecting *Hs*Prx3 to low pH (pH 4.2) by analogy to the work of Saccoccia et al. (2012). The low pH induced the formation of long, ordered helical filaments, as established by cryo-EM imaging and analysis. 3D reconstruction using single-particle analysis of helical *Hs*Prx3 revealed notable conformational differences relative to the available crystal structure of *Sm*Prx1 DS species. As seen in the stacked toroidal structure (Saccoccia et al., 2012), our study also establishes that the R interface plays a dominant role in *Hs*Prx3 nanotubes. Our study shows that the C-terminal region remains folded, as part of the intra-dimeric B interface. This observation is novel and in contrast to the unfolded C terminus deemed sterically necessary according to Saccoccia et al. (2012) who state "Unfolding of the C terminus, in turn, results in changes in the surface of the ring decamer at the R interface, allowing its interaction with another Prx decamer." In the light of the importance of the C terminus in (1) modulating the peroxidase function and (2) the formation of HMW during oxidative stress for other members of the 2-Cys family (Haynes et al., 2013), the clear distinction between *Sm*Prx1 and other 2-Cys Prxs in the pivotal C terminus suggests that *Sm*Prx1 is a special case. Thus, the sequence similarity of *Hs*Prx3 to other members of the 2-Cys Prxs at the C terminus and the observed similarity in the folding of the C terminus, as seen from our reconstruction compared with that in the available crystal structures of other 2-Cys Prxs, suggests that the *Hs*Prx3 helical filament is more representative of the HMW form for 2-Cys Prxs.

As an aside, our study also points at structural artifacts introduced by His-tags. The use of His-tags for purification is often assumed to have no effect on protein structure (Chant et al., 2005), due to its small size and lack of charge (Li, 2010). The pK_a of histidine is 6.0 (Dawson et al., 1969), which means that at physiological pH it is mostly deprotonated and uncharged. However, it has been shown that the use of a His-tag can in some cases influence protein structure or activity (Carson et al., 2007). In the case of Prxs, it can have a dramatic effect on their quaternary structure, seemingly stabilizing the toroidal oligomer (Cao et al., 2007) and significantly reducing peroxidase activity. Despite that, the presence of a His-tag has until now received no attention when analyzing HMW structures. While the crystal structure of *Sm*Prx1 DS revealed important pH-induced conformational changes, it is becoming clear that the His-tag has a major role in toroid association. We have observed a batch-to-batch variation in the ability of *Hs*Prx3 to form long filaments in the presence of a His-tag and double stacks similar to the ones seen for *Sm*Prx1 appeared to be the dominant species. We speculate that His-tags can affect the protein fold and promote a tight association between the N terminus and β-hairpin, which possibly prevents necessary conformational rearrangement thus locking it in a short DS state (Gretes and Karplus, 2013).

Putative Chaperone Model

Saccoccia et al. (2012) have proposed that, as a consequence of the disordered C terminus in DS, the LU active-site hydrophobic pocket becomes accessible and this might acts as the primary holdase site along with possible hydrophobic interactions by the unfolded C terminus in a manner similar to that seen in *Hs*Prx2/sulfiredoxin interaction (Jönsson et al., 2008). To check whether the partially folded C terminus provides a hydrophobic patch as seen for DS, we did a rigid-body fitting of a homology model of the *Hs*Prx3 monomer with the C terminus taken from the *Hs*Prx2 crystal structure (PDB: 1QMV) and generated a hydrophobic surface in UCSF Chimera (Pettersen et al., 2004) as shown in Figure 5 (Kyte et al., 1982). This exercise showed that the folded C terminus shielded the active-site hydrophobic patches on the external face of the filament (Figure 5A). However, we do observe extensive hydrophobic patches on the luminal face (Figure 5B). Angelucci et al. (2013) have proposed that the rim of the DS toroid

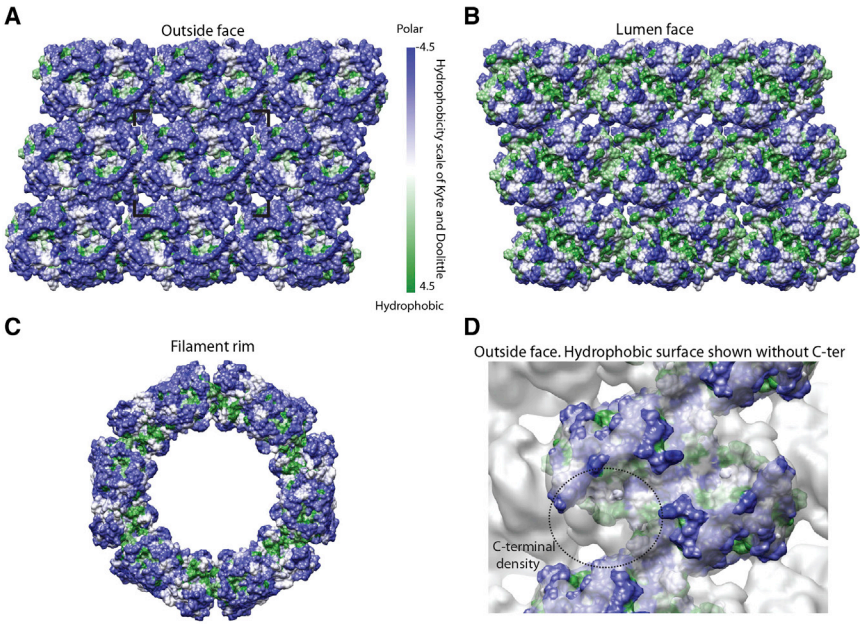

Figure 5. Hydrophobic Patches on the *Hs*Prx3 Filament

The polar characteristics of the 3D structure based on the pseudo-atomic model and visualized by unrolling the curved surface and viewed perpendicular to the helix axis to show the external (A) and luminal (B) surface shows that the rim (C) of the filament does not display as extensive hydrophobic patches as the luminal surface. The 3D model contained the C terminus explicitly (using that for the *Hs*Prx2 X-ray structure) in the renditions shown in (A), (B), and (C) but not in (D) in order to highlight the extra density attributable to a part of the C terminus (circle). The blue and green colors represent the polar and hydrophobic residues, respectively, as defined by the Kyte and Doolitle hydrophobicity scale (Kyte et al., 1982).

is hydrophobic, providing an entry site similar to that in GroEl. In our reconstructed 3D map of the filament, the rim extremity shows some hydrophobic patches (Figure 5C) but they are comparatively less extensive as in the lumen described above. We propose that the luminal hydrophobic patch in *Hs*Prx3 filaments (Figure 5) that we observe can impart holdase activity for the HMW form. The flexibility of the toroids (as exemplified by Figure 2) and the fact that filaments of various lengths can be formed could have a role in adapting to various cargo sizes. Furthermore, we note that the C terminus is implicated in the switch from holdase to peroxidase activity as indicated by its ability to unfold and interact with sulfiredoxin, a process by which the conversion from the hyperoxidized to the oxidized form takes place. This interaction dissociates the HMW to LMW form (Moon et al., 2013) and can be the mechanism of releasing the cargo.

The exact structure and function of HMW Prxs in vivo has not yet been unequivocally established. Our cryo-EM study, nevertheless, establishes that long filaments have important conformational distinction from the DS species as visualized by X-ray crystallography particularly at the C terminus. In conclusion, the 3D structure of the *Hs*Prx3 filament presents for the first time a model for the formation of long filaments that could be accessible to other 2-Cys Prxs. The structure shows extensive hydrophobic patches in the luminal surface that could facilitate its putative chaperone activity. The assembly-promoting interactions that we have visualized provide a framework for the design of targeted scrutiny of possible biological roles of Prx3 filaments. Ultimately, in situ visualization is needed to help clarify the in vivo relevance of Prx filaments and their potential role as chaperone species.

EXPERIMENTAL PROCEDURES

Protein Expression, Purification, and Formation of Nanotubes

Protein expression was performed in Rosetta (DE3) cells (Novagen) as described (Phillips et al., 2014). Cells were lysed in binding buffer (20 mM HEPES, 150 mM NaCl, 10 mM imidazole, pH 8.0) using a cell press (Microfluidics M110-P lab homogenizer) and the soluble fraction was subjected to affinity purification using a 5-ml HisTrap FF column (GE Healthcare). Fractions containing the *Hs*Prx3 protein were subjected to gel filtration using a HiLoad 16/60 Superdex 200 column (GE healthcare) using 20 mM HEPES, 150 mM NaCl (pH 8.0) buffer for further purification. The His-tag was cleaved by incubation with 1 μg of rTEV protease per mg of *Hs*Prx3 protein at 4°C for 24 hr in the presence of 2 mM β-mercaptoethanol. rTEV protein-cleaved His-tag and uncleaved protein were removed using a 1-ml HisTrap column (GE Healthcare) and the collected fractions were checked by SDS-PAGE. For tube formation, *Hs*Prx3 samples were acidified by dilution into low pH buffer (20 mM HEPES [pH 4], 75 mM NaCl) to a final protein concentration of 1 mg/ml.

Cryo-EM of Nanotubes and Image Processing

Frozen-hydrated specimens were prepared on glow-discharged holey EM grids (Quantifoil R2/2) using a Vitrobot Mark IV (FEI) with a 3-s blotting time at 100% humidity. Images were collected on a Tecnai TF20 electron microscope (FEI) operated at 200 kV using a Gatan cryo-holder and low-dose conditions (total dose of ~15 electrons per Å^2). Images were recorded on Kodak SO-163 films at a nominal magnification of 50,500×, and developed in D19 (Kodak) diluted 1:1 with deionized water for 10 min. Electron micrographs were digitized using a Nikon LS-9000 film scanner at a step size of 6.35 μm corresponding to 1.26 Å on the specimen.

The reconstruction of *Hs*Prx3 filament was performed in three main steps, as detailed below. First, a reconstruction without helical symmetry imposition was performed in order to calculate ab initio estimates of the helical symmetry parameters as described (Heymann et al., 2013). Second, these helix parameters were refined using IHRSR and additional tools for helical symmetry determination and imposition (Egelman, 2000). The refined parameters were then used to generate the final reconstruction using alignment restraints adapted to helical geometry and an improved symmetrization procedure with the software SPRING (Desfosses et al., 2014).

In the first step, *Bsoft* and EMAN2 were used to process a subset of the data (ten micrographs) and the whole dataset (45 micrographs), respectively. For processing in *Bsoft*, the contrast transfer function (CTF) parameters were automatically estimated using *fit_ctf* and manually adjusted for optimal fit to the experimental CTF plot. Filaments were picked using the *filament picker* module, and segmented into 7,572 segments of 320 × 320 pixels with 90% overlap using *bfil*. Using a featureless cylinder as a reference volume, an orientation search of the CTF-corrected segments was performed using the projection-matching algorithm embodied in *borient*, using imposition of C6 symmetry, determined previously (Phillips et al., 2014). The resulting reconstruction was next refined using EMAN2. A larger dataset of 42,982 segments of 320 × 320 pixels was generated with 90% overlap from filaments picked in

e2helixboxer, CTF-corrected, and used for refinement using *e2refine_easy*. C6 symmetry was imposed and the orientation search was restricted to ±10° for the out-of-plane tilt. The resulting reconstruction showed a clear helical nature, which was quantified using real-space autocorrelation methods described earlier (Heymann et al., 2013), giving initial symmetry parameters for axial rise and azimuthal rotation angle.

In the second step, further refinement of the helix parameters using the IHRSR approach (Egelman, 2000) was carried out varying the initial helical rise in values from 41 to 43 Å (in steps of 1 Å) and azimuthal rotation angles from 6° to 10° (in steps of 1°). More specifically, for each of the 15 pairs searched, refinement with SPIDER (Frank et al., 1996) included 60 iterations, using an initial model of a smooth cylinder 180 Å in diameter. The refinement was carried out using the *hsearch* program after the second round of iteration, using a step size of 0.01 Å for helical rise and of 0.1° for azimuthal rotation angle. The step size for azimuthal rotation was progressively brought down from 0.1° to 0.01° for the last ten iterations. The reconstructions obtained with the refined helix parameters showed a dihedral symmetry D6, as in the crystal structure of the dodecameric *Bt*Prx3 (PDB: 1ZYE) and was therefore imposed in further steps of refinement.

In the last step, we used the refined helix parameters to generate the final high-resolution reconstruction by applying the processing software dedicated to helical particles as encoded in SPRING (Desfosses et al., 2014). The CTF parameters were re-estimated for each micrograph using *ctffind* and *ctftilt*. Filament images were boxed into larger segments of 480 × 480 pixels, with a relatively large distance of 215 Å between each segment along the filament. This was done to make more use of the multiple inclusion of each segment in the 3D reconstruction according to the helical symmetry, which is a particular feature of the reconstruction algorithm described in (Sachse et al., 2007) and implemented in SPRING. The resulting 7,795 segments were corrected for the contribution of CTF and used in the automated reconstruction protocol of the *segmentrefine3d* module, using the independent refinement of two half sets, starting from a smooth cylinder to calculate the final FSC curve (the so-called gold standard FSC). For visual display and fitting, the EM map was filtered to 7 Å and sharpened using a B factor of $-300/Å^2$. Visualization and analysis of the 3D reconstructions were carried out using tools in *BSOFT*, *EMAN2*, *SPRING*, and UCSF Chimera. The homology model of the *Hs*Prx3 used for fitting was obtained using the I-TASSER server (Roy et al., 2010).

ACCESSION NUMBERS

Electron density map data have been deposited in the Electron Microscopy Data Bank (EMD: 6309).

SUPPLEMENTAL INFORMATION

Supplemental Information includes two figures and can be found with this article online at http://dx.doi.org/10.1016/j.str.2015.03.019.

AUTHOR CONTRIBUTIONS

M.R., J.A.G., and A.K.M. designed the experiments. A.J.P. and N.A.Y. expressed and purified the proteins. M.R. recorded the cryo-EM images. H.V. and A.D. did the image processing and reconstruction. H.V., A.D., M.R., and A.K.M. analyzed the data. M.B.H. provided the initial plasmid constructs and provided input into the biological aspects of the work in the text. M.R., H.V., A.D., J.A.G., and A.K.M. wrote the manuscript and all the authors commented on it.

ACKNOWLEDGMENTS

This work was supported in part by grants from the New Zealand Royal Society Marsden Fund and Health Research Council (A.K.M., M.B.H.) and the US Army Research Office and MacDiarmid Institute (J.A.G.). We thank Bernard Heymann regarding the use of Bsoft, and much helpful advice at the early stages of this work. We thank Adrian Turner for the maintenance of the EM suite at the School of Biological Sciences and Sina Masoud Ansari, Martin Feller, and Peter Maxwell for their help in implementing the EM processing software on the University of Auckland NESI pan cluster and organizing access to this cluster for computational resources for this work.

Received: January 2, 2015
Revised: March 21, 2015
Accepted: March 23, 2015
Published: April 23, 2015

REFERENCES

Angelucci, F., Saccoccia, F., Ardini, M., Boumis, G., Brunori, M., Di Leandro, L., Ippoliti, R., Miele, A.E., Natoli, G., Scotti, S., and Bellelli, A. (2013). Switching between the alternative structures and functions of a 2-Cys peroxiredoxin, by site-directed mutagenesis. J. Mol. Biol. *425*, 4556–4568.

Ardini, M., Giansanti, F., Di Leandro, L., Pitari, G., Cimini, A., Ottaviano, L., Donarelli, M., Santucci, S., Angelucci, F., and Ippoliti, R. (2014). Metal-induced self-assembly of peroxiredoxin as a tool for sorting ultrasmall gold nanoparticles into one-dimensional clusters. Nanoscale *6*, 8052–8061.

Cao, Z., Bhella, D., and Lindsay, J.G. (2007). Reconstitution of the mitochondrial PrxIII antioxidant defence pathway: general properties and factors affecting PrxIII activity and oligomeric state. J. Mol. Biol. *372*, 1022–1033.

Carson, M., Johnson, D.H., McDonald, H., Brouilett, C., and DeLucas, L.J. (2007). His-tag impact on structure. Acta Crystallogr. D Biol. Crystallogr. *63*, 295–301.

Chant, A., Kraemer-Pecore, C.M., Watkin, R., and Kneale, G.G. (2005). Attachment of a histidine tag to the minimal zinc finger protein of the *Aspergillus nidulans* gene regulatory protein AreA cause a conformational change at the DNA-binding site. Protein Exp. Purif. *39*, 152–159.

Cox, A.G., Winterbourn, C.C., and Hampton, M.B. (2009). Mitochondrial peroxiredoxin involvement in antioxidant defence and redox signalling. Biochem. J. *425*, 313–325.

Dawson, R.M.C., Elliott, D.C., Elliott, W.H., and Jones, K.M. (1969). Data for Biochemical Research. (Oxford University Press), pp. 103–114.

Desfosses, A., Ciuffa, R., Gutsche, I., and Sachse, C. (2014). SPRING - an image processing package for single-particle based helical reconstruction from electron cryomicrographs. J. Struct. Biol. *185*, 15–26.

Egelman, E.H. (2000). A robust algorithm for the reconstruction of helical filaments using single-particle methods. Ultramicroscopy *85*, 225–234.

Frank, J.L., Radermacher, M., Penczek, P., Zhu, J., Li, Y., Ladjadj, M., and Leith, A. (1996). SPIDER and WEB: processing and visualization of images in 3D electron microscopy and related fields. J. Struct. Biol. *116*, 190–199.

Gourlay, L.J., Bhella, D., Kelly, S.M., Price, N.C., and Lindsay, J.G. (2003). Structure-function analysis of recombinant substrate protein 22kDa (SP-22). A mitochondrial 2-Cys peroxiredoxin organized as a decameric toroid. J. Biol. Chem. *278*, 32631–32637.

Gretes, M.C., and Karplus, P.A. (2013). Observed octameric assembly of a *Plasmodium yoelii* peroxiredoxin can be explained by the replacement of native "ball-and-socket" interacting residues by an affinity tag. Protein Sci. *22*, 1445–1452.

Hall, A., Karplus, P.A., and Poole, L.B. (2009). Typical 2-Cys peroxiredoxins: structures, mechanisms and functions. FEBS J. *276*, 2469–2477.

Hall, A., Nelson, K., Poole, L.B., and Karplus, P.A. (2011). Structure-based insights into the catalytic power and conformational dexterity of peroxiredoxins. Antioxid. Redox Signal. *15*, 796–815.

Harris, J.R. (1968). Release of a macromolecular protein component from human erythrocyte ghosts. Biochim. Biophys. Acta *150*, 534–537.

Haynes, A.C., Qian, J., Reisz, J.A., Furdui, C.M., and Lowther, W.T. (2013). Molecular basis for the resistance of human mitochondrial 2-Cys peroxiredoxin 3 to hyperoxidation. J. Biol. Chem. *288*, 29714–29723.

Heymann, J.B., Bartho, J.D., Rybakova, D., Venugopal, H.P., Winkler, D.C., Sen, A., Hurst, M.R., and Mitra, A.K. (2013). Three-dimensional structure of the toxin-delivering particle antifeeding prophage of *Serratia entomophila*. J. Biol. Chem. *288*, 25276–25284.

Hofmann, B., Hecht, H.J., and Flohé, L. (2002). Peroxiredoxins. Biol. Chem. *383*, 347–364.

Jang, H.H., Lee, K.O., Chi, Y.H., Jung, B.G., Park, S.K., Park, J.H., Lee, J.R., Lee, S.S., Moon, J.C., Yun, J.W., et al. (2004). Two enzymes in one; two yeast peroxiredoxins display oxidative stress-dependent switching from a peroxidase to a molecular chaperone function. Cell *117*, 625–635.

Jönsson, T.J., Johnson, L.C., and Lowther, W.T. (2008). Structure of the sulphiredoxin-peroxiredoxin complex reveals an essential repair embrace. Nature *451*, 98–101.

Kil, I.S., Lee, S.K., Ryu, K.W., Woo, H.A., Hu, M.-C., Bae, S.H., and Rhee, S.G. (2012). Feedback control of adrenal steroidogenesis via H_2O_2-dependent, reversible inactivation of peroxiredoxin III in mitochondria. Mol. Cell *46*, 584–594.

Kumsta, C., and Jakob, U. (2009). Redox-regulated chaperones. Biochemistry *48*, 4666–4676.

Kyte, J., Doolittle, R.F., Diego, S., and Jolla, L. (1982). A simple method for displaying the hydropathic character of a protein. J. Mol. Biol. *157*, 105–132.

Li, Y. (2010). Commonly used tag combinations for tandem affinity purification. Biotechnol. Appl. Biochem. *55*, 73–83.

Moon, J.C., Hah, Y.-S., Kim, W.Y., Jung, B.G., Jang, H.H., Lee, J.R., Kim, S.Y., Lee, Y.M., Jeon, M.G., Kim, C.W., et al. (2005). Oxidative stress-dependent structural and functional switching of a human 2-Cys peroxiredoxin isotype II that enhances HeLa cell resistance to H_2O_2-induced cell death. J. Biol. Chem. *280*, 28775–28784.

Moon, J.C., Kim, G.M., Kim, E.-K., Lee, H.N., Ha, B., Lee, S.Y., and Jang, H.H. (2013). Reversal of 2-Cys peroxiredoxin oligomerization by sulfiredoxin. Biochem. Biophys. Res. Commun. *432*, 291–295.

Pettersen, E.F., Goddard, T.D., Huang, C.C., Couch, G.S., Greenblatt, D.M., Meng, E.C., and Ferrin, T.E. (2004). UCSF Chimera–a visualization system for exploratory research and analysis. J. Comp. Chem. *25*, 1605–1612.

Phillips, A.J., Littlejohn, J., Yewdall, N.A., Zhu, T., Valéry, C., Pearce, F.G., Mitra, A.K., Radjainia, M., and Gerrard, J.A. (2014). Peroxiredoxin is a versatile self-assembling tecton for protein nanotechnology. Biomacromolecules *15*, 1871–1881.

Roy, A., Kucukural, A., and Zhang, Y. (2010). I-TASSER: a unified platform for automated protein structure and function prediction. Nat. Protoc. *5*, 725–738.

Saccoccia, F., Di Micco, P., Boumis, G., Brunori, M., Koutris, I., Miele, A.E., Morea, V., Sriratana, P., Williams, D.L., Bellelli, A., and Angelucci, F. (2012). Moonlighting by different stressors: crystal structure of the chaperone species of a 2-Cys peroxiredoxin. Structure *20*, 429–439.

Sachse, C., Chen, J.Z., Coureux, P.D., Stroupe, M.E., Fändrich, M., and Grigorieff, N. (2007). High-resolution electron microscopy of helical specimens: a fresh look at tobacco mosaic virus. J. Mol. Biol. *371*, 812–835.

Teixeira, F., Castro, H., Cruz, T., Tse, E., Koldewey, P., Southworth, D.R., Tomás, A.M., and Jakob, U. (2015). Mitochondrial peroxiredoxin functions as crucial chaperone reservoir in *Leishmania infantum*. Proc. Natl. Acad. Sci. USA *112*, E616–E624.

Wang, X., Wang, L., Wang, X., Sun, F., and Wang, C. (2012). Structural insights into the peroxidase activity and inactivation of human peroxiredoxin 4. Biochem. J. *441*, 113–118.

Winterbourn, C.C., and Hampton, M.B. (2008). Thiol chemistry and specificity in redox signaling. Free Radic. Biol. Med. *45*, 549–561.

Wood, Z.A., Poole, L.B., Hantgan, R.R., and Karplus, P.A. (2002). Dimers to doughnuts: redox-sensitive oligomerization of 2-cysteine peroxiredoxins. Biochemistry *41*, 5493–5504.

Wood, Z.A., Schröder, E., Harris, J.R., and Poole, L.B. (2003). Structure, mechanism and regulation of peroxiredoxins. Trends Biochem. Sci. *28*, 32–40.

Zhang, Y. (2008). I-TASSER server for protein 3D structure prediction. BMC Bioinformatics *9*, 40.

 ©2015 Elsevier Ltd All rights reserved